

Drift, shape, and intrinsic destabilization of pulses of traveling-wave convection

Paul Kolodner

AT&T Bell Laboratories, Murray Hill, New Jersey 07974-0636

(Received 18 April 1991)

I describe experiments on “pulses” of convective traveling waves in an annular geometry, using ethanol-water mixtures with moderate negative separation ratio. In a sufficiently uniform cell at constant Rayleigh number, pulses drift in the direction of propagation of the underlying traveling waves, with no long-term change in velocity. The drift velocity increases with increasing distance ϵ above onset. In contrast with previous observations of *motionless* pulses, this result is qualitatively consistent with theories based on a subcritical Ginzburg-Landau equation. The pulse shape is also described in detail. The pulses exhibit a noticeable asymmetry, which decreases as ϵ is increased. I also describe experiments at high ϵ in which pulse destruction by convective amplification of traveling-wave fluctuations is suppressed by the existence of multiple pulses. In this case, destabilization takes place by an intrinsic mechanism: Above a certain threshold, the pulse simply expands into the rest of the system, accompanied by a large decrease in wave speed.

PACS number(s): 47.25.Qv, 47.20.Ky

I. INTRODUCTION

One of the most interesting features of one-dimensional traveling-wave (TW) convection in binary fluid mixtures is the tendency of this system to exhibit *confined states*: spatially isolated regions of TW's which coexist stably with the rest of the system, which is quiescent [1–3]. Confined states were first observed in narrow rectangular convection cells, using fluids with separation ratio $\psi \sim -0.1$ [1]. The fact that confined states appeared near the end walls of the cell, coupled with their similarity to states produced by a theoretical model based on coupled Ginzburg-Landau equations which explicitly included the reflections of TW's from the walls [4], suggested that such reflections were important to their existence. However, the recent observation of the same confined state in narrow annular cells [2,3], in which there are no reflections, has cast doubt on such an interpretation. The careful measurements in Ref. [2], in particular, have shown that this confined state bears a strong resemblance to a “pulse” solution of a subcritical Ginzburg-Landau equation for the amplitude of unidirectional, one-dimensional TW's in an unbounded geometry [5,6]. Thus it appears correct to refer to the confined state seen near $\psi \sim -0.1$ in a narrow experimental geometry as a pulse i.e., a state whose confinement is an intrinsic feature of the unbounded system and not caused by the interaction of TW's with the end walls of the cell.

However, despite the resemblance of experimental pulses to solutions of subcritical Ginzburg-Landau equations, they exhibit two features which are not given by this model. The first is their stability above onset. In an infinite system [6], a pulse solution is stable only up to value $\epsilon_3 \leq 0$ whose value depends on system parameters (here ϵ denotes the fractional distance above the onset of convection). For parameters such that $\epsilon_3 < 0$, the pulse goes unstable by splitting into two fronts which expand into the rest of the system at a selected velocity which

vanishes at ϵ_2 and increases monotonically for $\epsilon > \epsilon_3$. In the Benjamin-Feir unstable regime [6], the state between the expanding fronts exhibits phase defects. The experimental behavior is quite different. In annular containers, experimental pulses are observed to be stable over a band of Rayleigh numbers which straddles the onset of convection and extends to $\epsilon_f \sim 0.01$ [2,3,7]. Above this value, my collaborators and I have shown that pulse destabilization in an annulus occurs because of destruction by convectively amplified fluctuations [7]. In a rectangular geometry, where these fluctuations are suppressed by losses upon reflection from the end walls of the cell, I have recently found [8] that pulses do go unstable via a mechanism which bears some resemblance to the scenario predicted in Ref. [6]. However, pulse stability *above onset* still seems to contradict the theory valid for an infinite system.

The second perplexing feature of traveling-wave pulses is that, except for transients, previous experiments found them to be motionless in the laboratory frame [2,3,7], whereas pulse solutions of the simplest subcritical Ginzburg-Landau equation implicitly drift at the group velocity s_0 of linearly unstable TW's [5,6]. It should be stressed that this linear group velocity is large: for typical experimental conditions, $s_0 \sim 1.5$ in dimensionless units, while the largest transient pulse drift velocity observed in experiments prior to the present work is $\lesssim 0.02$ [9]. In general, it is a surprise to find that a system which exhibits continuous translational symmetry should select a pulse velocity of zero for a wide range of parameters. In an attempt to reconcile these observations, Deissler and Brand [10] numerically investigated the effect of adding cubic nonlinear gradient terms to the Ginzburg-Landau equation. They found that such terms can indeed slow and even reverse the propagation of pulses. In addition, a pronounced asymmetry in pulse shape was observed. However, in a single-field Ginzburg-Landau theory, a vanishing pulse velocity occurs only for a

measure-zero set of parameters. This contradicts previous observations of stationary pulses for a wide range of experimental parameters.

A great deal of insight into traveling-wave pulses has been shed by the recent work of Barten, Lücke, and Kamps [11]. These authors performed numerical integrations of the full, two-dimensional Navier-Stokes equations which govern convection in binary fluids. One of the solutions they found, for $\psi = -0.08$, appeared to be identical to experimentally observed pulses. Significantly, they found that this pulse solution was accompanied by a large-scale circulation of concentration which affects the buoyant forces in the fluid in such a way as to reduce the pulse propagation velocity to a value 35 times lower than the linear group velocity, for $\epsilon = 0.008$. The difference between this slow propagation and zero velocity seems small, and the authors suggested that the influence of the side walls of experimental cells—typically, cells are only 1.5 to 2 times wider than their height—may account for previous experimental observations that pulses do not drift. However, both of the important effects discussed in that work—large-scale flows and the influence of side walls—lie outside the scope of subcritical Ginzburg-Landau models.

In this paper, I report experimental observations of pulses of traveling-wave convection in an annular geometry. The distinguishing feature of these experiments is that a significant effort has been expended in assessing and reducing nonuniformities in the convection cell. In contradiction to previous reports, I find that, in a sufficiently uniform cell, traveling-wave pulses do drift [12]. The drift velocity v_{dr} vanishes near onset, exhibits a shifted square-root dependence on the distance ϵ above onset, and agrees fairly well with the drift velocity found in Ref. [11]. Drift velocities as high as 0.08 have been observed. The parameters of the fitted dependence $v_{dr}(\epsilon)$, as well as the value ϵ_2 below which pulses lose stability and vanish, depend on the separation ratio ψ . Because of the sensitivity of drift velocity on ϵ , the pulse drift follows local nonuniformities in the convection cell. It is necessary to postulate only a rather modest level of nonuniformity for there always to exist a region in the cell where pulses exhibit zero velocity for any applied temperature difference for which they are stable. Under such conditions, pulses exhibit a transient drift until they reach this region, at which time they stop, and this appears to be what has happened in previous experiments. The challenge I now present to theorists is to calculate the dependence of the drift velocity on ϵ and on ψ .

A second feature of the pulses described in this paper is their shape. Niemela, Ahlers, and Cannell [2] found that pulse profiles could be fit using a function which is a zero-drift-velocity solution to the lowest-order subcritical Ginzburg-Landau equation. This stationary analytical pulse exhibits a spatially symmetric amplitude profile. However, in theory [6], pulses which drift exhibit a spatial asymmetry, and this feature was observed in both the numerical work of Barten, Lücke, and Kamps [11] and the simulations of Deissler and Brand [10]. Motivated by this apparent discrepancy, I have performed a detailed analysis of pulse shape for a subset of my data. The

pulses observed in these experiments do indeed exhibit an asymmetry, associated dominantly with a leading-edge shoulder. This asymmetry decreases sharply with ϵ . The pulse shape appears to be very well described by the numerical pulse of Ref. [11].

This paper also includes a brief account of observations of the destabilization of traveling-wave pulses. As mentioned above, this destabilization is usually the result of the interaction between pulses and convectively amplified TW fluctuations. However, as pointed out in Ref. [7], while pulses are destroyed by large-amplitude fluctuations, they are total absorbers of small-amplitude TW's. Thus, by creating several pulses in the same cell, I have been able to extend the range of stability against fluctuations to larger values of ϵ than have been achieved in previous experiments. This has allowed the observation of quite rapidly drifting pulses, since the pulse velocity increases monotonically with ϵ . More importantly, the suppression of fluctuations in states consisting of three pulses is so complete that the threshold for pulse destabilization via an intrinsic mechanism can be reached. This mechanism consists of the pulse splitting into two fronts which expand into the rest of the system, in qualitative agreement with analytical work based on the subcritical Ginzburg-Landau equation [6]. However, at the same time, the velocity of the underlying TW drops substantially.

The remainder of this paper is organized as follows. Sections II and III describe the experimental apparatus and the use of states of linear TW's as diagnostics for cell uniformity and geometry. In Sec. IV, I describe techniques for creating multiple pulses, and I present pulse-drift data. Section V describes measurements of pulse shape, and Sec VI deals with intrinsic destabilization of pulses. Section VII is a summary.

II. APPARATUS

The convection cell used in these experiments, shown in Fig. 1, has evolved from the cells used in several previous experiments [7] and has been designed for extreme geometric and thermal uniformity. The bottom plate is a mirror-polished disk of silicon, of thickness 1.524 cm, to the bottom of which has been glued an electrical film heater. The walls of the cell are formed by a disc and ring of ULTEM 1000 polyetherimide plastic which have been turned on a lathe so as to key to a center hole and outer lip in the silicon plate. Because of this, the walls of the cell are accurately concentric. The top plate of the cell is an extremely flat disk of sapphire of thickness 0.635 cm. The cell is sealed by four flat gaskets of ethylene-propylene rubber which sit in grooves just outside the walls of the cell, and two small, diametrically opposite holes at mid-height are connected to Teflon tubes (not shown) for filling the cell. Three versions of this cell were used in this work, differing in the dimensions of the plastic spacers and the geometric uniformity which was achieved. Their dimensions are listed in Table I.

Silicon has several advantages over polished metal mirrors for experiments of this type. This material does not need to be plated for protection or reflectivity, can be

TABLE I. Fluid properties and cell dimensions. $\Gamma_{r,\phi}$ is the radial width and mean circumference of the cell, scaled by its height. ψ , P , and L are the separation ratio, Prandtl number, and Lewis number, respectively.

Cell	Height (cm)	Γ_r	Γ_ϕ	c (wt %)	T_{mean} (° C)	ψ	P	L
A	0.3130(21)	1.655(11)	75.96(50)	0.0145	26.9	-0.072	6.69	0.0086
B	0.2680(9)	1.876(6)	88.67(30)	0.0220	27.9	-0.101	6.83	0.0087
C	0.2582(4)	1.948(3)	92.03(14)	0.0280	28.2	-0.123	7.00	0.0088

easily polished to extreme flatness, and is quite difficult to scratch or corrode. Thus the disassembled mirror can be cleaned by buffing vigorously, and the assembled cell can be flushed with concentrated hydrochloric acid. The disadvantages of reduced thermal conductivity and optical reflectivity, with respect to nickel-plated copper or sterling silver, have proven to be unimportant.

The cell is clamped together between two circular brass frames. The upper frame serves as a flow channel for the circulating water which cools the top of the sapphire plate and as a holder for the upper quartz window and the main lens of the optical system. As shown in Fig. 1, cooling water is injected tangentially at two points into an annular channel of rectangular cross section which has been cut into the underside of the upper frame. A gap of 0.013 cm between the bottom face of the inner wall of this channel and the sapphire plate allows cooling water to leak out onto the sapphire with substantial azimuthal velocity, swirling around and cooling the cell in an azimuthally symmetric manner. A larger gap at the top window of the flow channel allows the water to pass into an upper annular channel, from which it returns to its source. The cell assembly sits on leveling screws and is surrounded by insulating foam.

The geometric uniformity of the convection cell has

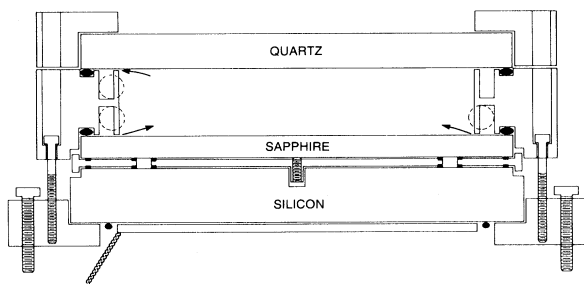


FIG. 1. A cross section of the experimental cell is shown. The cell is formed by a plastic disk and ring which are clamped between a silicon bottom plate and a sapphire top plate. Cooling water is injected into the space above the cell, following the paths indicated by arrows. A film heater is glued to the bottom of the silicon plate; in addition, a ring of small resistors (shown as two black dots on either side of the main heater) has been attached to the outside edge of this plate, for trimming out small asymmetries in the bottom-plate temperature. The main lens of the optical system (not shown) is attached to the frame of the top quartz window, and the entire cell is surrounded by thick foam insulation (also not shown).

been assessed using several mechanical, optical, and convective techniques. The diameter of the outer cell wall was measured to an accuracy of about 5×10^{-4} cm using a calibrated, three-point inside-diameter micrometer. The radial width of the cell was measured at eight different places using an optical comparator, which has reproducibility of about 2×10^{-4} cm. From these measurements, I obtain a very accurate measurement of the mean diameter and width of the cell, and I verify that the width exhibits azimuthal nonuniformities of less than about 3×10^{-4} cm. This is small enough to be unimportant. The thickness of the cell spacer is measured using a micrometer, but, because the sealing gaskets might not be squeezed completely into their grooves when the cell is clamped together, this does not necessarily represent the true height of the assembled cell. As described in Sec. III, the properties of linear TW's can give a potentially more accurate indication of the average cell height, and the dimensions in Table I were deduced this way. Finally, the uniformity of the height of the cell is assessed by performing the final assembly under an interferometer which is installed in the experimental optical system. By tightening the twelve screws which hold the cell together against the resistance of the sealing gaskets, I can make minute local adjustments of the cell height. In this way, the height can be adjusted with a uniformity of as good as \pm one fringe, representing a fractional height uniformity of about $\pm 1 \times 10^{-4}$, and this figure remains stable for long times [13]. With noncompliant gaskets, the uniformity can easily be twenty times worse, and that is bad enough to have a substantial effect on all of the dynamical states discussed below.

The thermal control of the cell comes from the cooling water and the lower-plate heater. A bath circulator provides the input water, whose temperature (25.00°C) is regulated to a stability of about ± 0.6 mK by a dc-bridge-servo circuit driven by a thermistor in contact with the sapphire plate. A pair of thermistors, one in contact with the sapphire plate and the other embedded in the silicon plate, form two arms of an ac bridge whose output is used to regulate the power applied to the film heater on the lower plate. The short-term fluctuations of the difference temperature are measured using a separate dc bridge and are found to be about ± 0.15 mK. These numbers should be compared with the temperature difference applied across the cell during experimental runs, which is typically 5°C . The long-term fluctuations are more appropriately measured using the properties of linear TW's, as described below.

Direct assessment of the thermal uniformity of the cell

is rather difficult. A thermistor dragged in a circle across the top of the sapphire plate with a temperature difference applied across the cell did not reveal any nonuniformities at the level of a few mK but was not much more precise than that. Furthermore, a direct, nonperturbing measurement of the temperature profile of the lower plate seems quite difficult and has not been attempted. However, as I show below, both the properties of linear TW and the propagation of nonlinear TW pulses can be used for extremely sensitive measurements of the uniformity of the Rayleigh number.

The fluids used in these experiments are carefully degassed solutions of high-purity ethanol in deionized water. The fluid parameters are taken from Ref. [14] and are listed in Table I. Repeated flushing with fresh solutions and overnight stirring by fully nonlinear TW convection at moderate Rayleigh number are performed before commencing experiments, to ensure that accidental large-scale concentration gradients are eliminated.

The optical system used in these experiments, which has been described in detail in a previous publication [15], consists of a telescope which views the cell from above and projects a reduced white-light shadowgraph image of it, through beamsplitters, onto various detectors. One of these, referred to here as the circular camera, consists of an annular array of 720 wedge-shaped photodiodes. Since the convection patterns are one dimensional, consisting of radial wave fronts which propagate azimuthally, such a detector is ideal for sampling the image in space-time. Under the control of a small computer, the circular camera makes scans of the image at regular time intervals and stores them for later analysis. For pulse data, this analysis consists of computation of the pulse amplitude profile at each time step, using spatial demodulation at the measured mean wave number. In addition, the computer can calculate the profiles of the two oppositely propagating azimuthal components of the convection pattern in real time, using complex demodulation [15]. This capability is used in the analysis and control of linear TW states (see below). I refer to the two azimuthal directions of propagation in the annulus as "left" and "right." A second image of the shadowgraph is projected onto a video camera for inspection of the pattern, and a photomultiplier views a selectable point in a third image through a narrow slit.

III. LINEAR TRAVELING WAVES AS A DIAGNOSTIC TOOL

The linear instability which triggers the onset of convection in binary fluid mixtures has been extensively studied using experimental [16] and theoretical [17] techniques. In a uniform or nearly uniform one-dimensional system, the oscillations due to this instability consist of superpositions of left- and right-going TW's whose amplitudes $A_{L,R}(x,t)$ obey a linearized Ginzburg-Landau equation:

$$\tau_0 \left[\frac{\partial A_{L,R}}{\partial t} \pm s \frac{\partial A_{L,R}}{\partial x} \right] = \epsilon(x)(1 + ic_0) A_{L,R} + \xi_0^2 (1 + ic_1) \frac{\partial^2 A_{L,R}}{\partial x^2}. \quad (1)$$

In this equation, the stress parameter ϵ is allowed to have a weak spatial dependence, in order to account for nonuniformities in the experimental cell. I define $\bar{\epsilon}$ to be the spatial average of $\epsilon(x)$. Experimentally, $\bar{\epsilon}$ corresponds to the fractional amount by which the applied Rayleigh number exceeds the measured onset of convection. τ_0 is a characteristic growth time, s is the group velocity, and ξ_0 is a correlation length. The coefficients $c_{0,1}$ are very small for the fluids used in these experiments and will henceforth be neglected. These parameters have been calculated theoretically, and experiments have verified these calculations with high precision. Linear TW states can be stabilized at onset and experimentally characterized in great detail. Each experimental run in this work begins and ends with a careful observation of linear TW's, and this gives a great deal of useful diagnostic information.

The first piece of information obtained from linear TW's is the applied temperature difference corresponding to the onset of convection, which defines $\bar{\epsilon} \equiv 0$. To initiate this measurement, the temperature difference ΔT applied across the cell is set at the nominal onset measured previously, and a flexible metal bellows which terminates one of the cell's fill tubes is gently tapped. As described in Ref. [7], this causes fluid to squirt into and out of the two filling holes, creating disturbances in the cell at their locations. In a short time, each of these decomposes into two narrow, oppositely propagating linear wave packets which begin traveling around the cell (this process is illustrated in the presence of a nonlinear pulse in Fig. 6 below). In this way, linear wave "energy" is rapidly injected into the system, and, over the course of about two days, the narrow wave packets evolve into a pattern of nearly spatially uniform TW's. The measurement of the convective onset consists of servoing ΔT so that the total wave energy in the system exhibits a vanishing growth rate. To accomplish this, shortly after the wave packets are injected into the cell, the computer which controls the circular camera begins repetitively running a program which acquires data corresponding to a few oscillation periods and calculates the spatial profiles of the left- and right-going TW amplitudes. An analog signal proportional to the sum of the spatial averages of these two profiles is fed to the computer which controls ΔT , and this computer begins executing a servo program which adjusts ΔT so as to keep the analog signal constant. Because the input to the servo is a spatially averaged wave amplitude, this program converges on the onset of convection quite rapidly—the fractional fluctuations can drop to the 10^{-4} level in a few hours—even though the spatial structure of the TW continues to evolve for a day or two.

With a technique of this precision, onset measurements spaced a few weeks apart allow the detection of very small drifts, such as may be due to small leaks in the cell

plumbing. These can allow ethanol to selectively evaporate, changing the separation ratio, and hence the onset temperature, at a localized position in the cell. In the experiments reported here, the worst drifts in onset were only at the level of 1×10^{-4} per day, and this is negligible. In analyzing the pulse data, I subtracted out the measured drifts.

Once the TW pattern at onset has settled, its amplitude and wave-number profiles can be used for assessing the uniformity of the cell and the alignment of the optics. The profiles in Figs. 2(a) and 2(b) were measured using a fluid with $\psi = -0.021$ in cell *A*. The amplitude profiles in Fig. 2(a) are uniform to within $\pm 30\%$, and this is quite good. These measurements can be substituted into Eq. (1) to yield two separate estimates for the spatial dependence of the stress parameter ϵ :

$$\epsilon_{L,R}(x) = \pm \frac{s\tau_0}{A_{L,R}(x)} \frac{\partial A_{L,R}}{\partial x} - \frac{\xi_0^2}{A_{L,R}(x)} \frac{\partial^2 A_{L,R}}{\partial x^2}. \quad (2)$$

It should be pointed out that the group velocity s used in

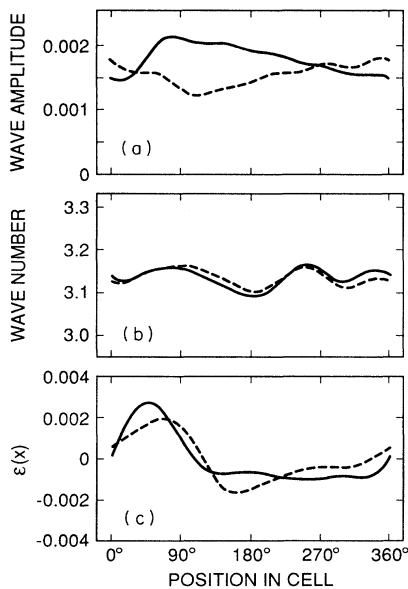


FIG. 2. Amplitude and wave-number profiles calculated vs position x in cell *A* by complex demodulation of circular-camera data, for a steady state of linear waves exactly at onset, using a fluid with $\psi = -0.021$. In all three frames, full curves correspond to the right-wave component, and dashed curves correspond to the left-wave component. (a) Amplitude profiles $A_{L,R}(x)$, measured in units of fractional image intensity. Both profiles exhibit spatial growth in the region 0° – 90° and spatial decay in the region 90° – 360° . (b) Wave-number profiles $k_{L,R}(x)$. The two wave numbers agree almost exactly and exhibit very slight distortions. (c) Local stress parameter $\epsilon_{L,R}(x)$ derived from the amplitude profiles in (a) using Eqs. (1) and (2). The two curves agree well and exhibit nonuniformities of better than about $\pm 0.2\%$.

these estimates is obtained by dividing the measured oscillation frequency by the measured wave number. Because of the narrow cell width, this value is somewhat smaller than the theoretical value [7,18]. By contrast, the parameter τ_0 , which has been deduced roughly from the dependence of growth rate on ΔT [16], does not appear to be affected by this. Also, the second term on the right-hand side of Eq. (2) is small, so the accuracy of the parameter ξ_0^2 is not important, and the theoretical value is used without further verification.

The estimates calculated using Eq. (2) are shown in Fig. 2(c). They agree reasonably and indicate that cell *A* exhibits nonuniformities in Rayleigh number of less than $\pm 0.2\%$. This value, while small, is still a few times larger than the calculated effect of the measured nonuniformity of the cell geometry on the local Rayleigh number. I therefore deduce that the source of this asymmetry is a nonuniform bottom-plate temperature, possibly caused by a defective or improperly positioned film heater. In cell *C*, an initial asymmetry in $\epsilon(x)$ comparable to that in Fig. 2(c) was corrected by gluing a ring of small heaters around the edge of the underside of the silicon bottom plate, as shown in Fig. 1, and adjusting the local heating. As described in a forthcoming article [19], a stable uniformity in $\epsilon(x)$ of $(1-3) \times 10^{-4}$ was achieved in this way.

The use of linear TW amplitude profiles for measuring the profile of $\epsilon(x)$ requires the convection pattern to have settled to a steady, single-azimuthal-mode state with both wave components exhibiting measurable amplitudes. I do not yet trust this method enough to believe $\epsilon_L(x)$ without corroboration from $\epsilon_R(x)$. Also, an implicit assumption in the derivation of Eq. (1) is that the amplitude profiles of TW's vary only slowly in space. Thus a narrow-bandwidth demodulator was used to compute the profiles in Fig. 1, and only the smoothest components of $\epsilon_{L,R}(x)$ can be measured. In cell *B*, which exhibited a very localized nonuniformity, the linear state obtained after several days consisted of a superposition of two modes, one strong and one weak, and this gave rise to a slowly modulated pattern from which stable profiles for $\epsilon_{L,R}(x)$ could not be calculated. However, as I show below, the ϵ dependence of the propagation of nonlinear pulses can also be used for a very reliable determination of the uniformity of the cell.

The wave-number profiles $k_{L,R}(x)$ of the linear TW's are also useful. The two wave-number profiles shown in Fig. 2(b) agree almost exactly, and their mean is uniform in space to within better than $\pm 1\%$. By changing the focalization distance and other parameters of the optical system, I have verified that these nonuniformities are due solely to misalignments and distortions in the optics and do not represent anything about the dynamics of the convective state. Therefore I have used the wave-number profiles as a diagnostic for the optics. The computer program which calculates the TW amplitude profiles also displays the sine and cosine components of the lowest spatial Fourier mode of the mean of the wave-number profiles. These differ from zero if the optical axis of circular camera is not centered on the image of the cell, and I adjust the transverse position of the camera to null them (the second and third harmonics represent distur-

tions due to misalignments of other optical components and to tilt of the circular camera, but I have not yet found a reliable way to use this information for optimization. With this adjustment, the nonuniformities in the wave-number profiles can be reduced to the level of $\pm 0.5\%$ in cells *A* and *C*. Once adjusted, this figure deteriorated to only $\pm 1\%$ after a month of experiments in cell *C*. In cell *B*, which exhibited only a modulated linear state, the amplitude of the lowest Fourier mode of the mean wave-number profile exhibited a small slow oscillation due to the beating of the two modes, and I adjusted the camera position to null the mean of the oscillations. Even in cell *B*, distortions and misalignments are too small to have a measurable affect on pulse drift.

One last piece of diagnostic information comes from the photomultiplier measurement of the image intensity at a single spatial point during the evolution of the linear TW pattern. Figure 3 shows temporal spectra computed from several subsets of such a time series. Figure 3(a), from a segment beginning shortly after the narrow wave packets were first injected into cell *A*, exhibits two dominant spectral lines of similar amplitude. These correspond to the two azimuthal spatial modes whose interference produces the wave packets which have evolved from

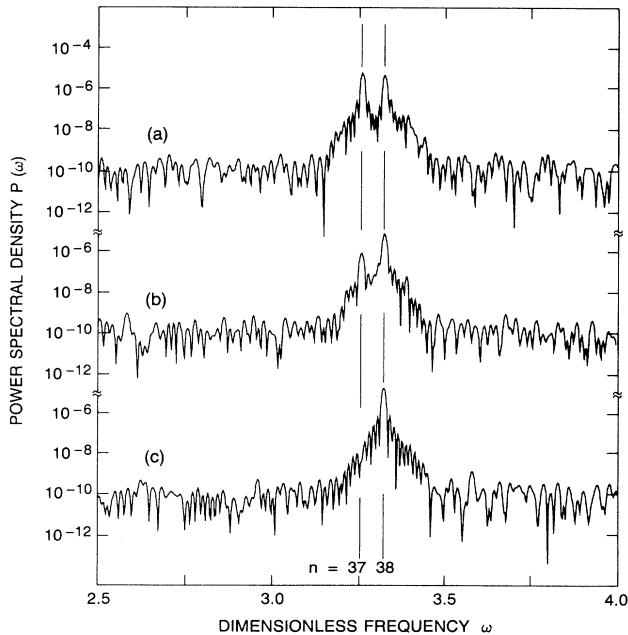


FIG. 3. Power spectra computed from three 20000-sec segments of a time series of single-point image-intensity measurements, during the evolution of a state of linear waves in the same fluid as in Fig. 2. The spectrum in (a) is derived from a segment beginning about 4 h after the injection of linear wave packets into the system and shows spectral lines corresponding to two azimuthal modes. In the time series used for (b), started 20000 sec after the end of that in (a), the lower mode has decayed. In (c), started 20000 sec after the end of that in (b), one mode remains, corresponding to the 38th azimuthal mode.

the initial localized disturbances. As time proceeds [Fig. 3(b)], one of the lines decays, leaving a single line [Fig. 3(c)] which, as verified from the circular-camera image, corresponds to an azimuthal mode number of $n = 38$.

The growth rate of the n th mode, whose wave number is k_n , can be deduced from Eq. (1):

$$\gamma_n = \tau_0^{-1} \bar{\epsilon} - \Delta k_n^2, \quad (3)$$

where $\Delta k_n = k_n - k_c$, and k_c is the critical wave number [16]. The relative growth of the different lines in a multi-line spectrum is thus an inverted parabola centered on the frequency corresponding to k_c , and a fit to such data can yield k_c , if more than two lines are present (note that, since linear TW's are practically dispersionless [16,17], a frequency spectrum is equivalent to a wave-number spectrum). Thus a fit to the relative growth rates in a three-line spectrum measured in cell *C* exhibited a maximum at a frequency corresponding to $n_c = 45.67 \pm 0.07$. However, even the two-line spectrum in Fig. 3 permits the deduction that, in cell *A*, k_c lies between wave numbers of the 37th and 38th modes and is closer to the latter. That is, the mode number corresponding to k_c is $n_c = 37.75 \pm 0.25$. With the theoretical value [17] $k_c/\pi - 1 = -0.0061$, this allows the dimensionless circumference of the cell to be deduced: $\Gamma_\phi = 2\pi n_c/k_c = 76.0 \pm 0.5$. Since the physical measurement of the mean circumference is quite accurate—for cell *A*, $\Gamma_\phi d = 23.776 \pm 0.003$ cm—this yields the cell height $d = 0.3130 \pm 0.0021$ cm. This is to be compared with the measured thickness of the spacer used in cell *A*: 0.3073 ± 0.0005 cm. The deduced value relies on the theoretical calculation of the critical wave number, which may not be accurate for the narrow cells used in this work [18]. However, averaged over the three cells, this value exceeds the measured spacer thickness by 0.0055 ± 0.0020 cm—an amount which believably corresponds to the resistance of the cell gaskets. In any event, using one of these values instead of the other would make a negligible change in the pulse velocities measured below.

IV. PULSE PRODUCTION AND DRIFT

In this system, for $\psi \sim -0.1$, the first stable nonlinear state observed upon increasing $\bar{\epsilon}$ above onset is one of traveling-wave pulses. The main qualitative effect studied in this paper is illustrated in Fig. 4: in a sufficiently uniform cell, pulses drift continuously in the direction of the underlying TW. This drift is not a transient. I have observed pulses to drift for days at constant $\bar{\epsilon}$, with no long-term change in velocity. As shown below, the drift velocity depends on the local value of $\epsilon(x)$ and thus on the spatially averaged value $\bar{\epsilon}$. The fastest pulses studied circle the cell in 24 h. Using techniques described below, I have made states consisting of one, two, and three copropagating pulses. At the same $\epsilon(x)$, pulses in multiple-pulse states propagate at the same velocity as they do in single-pulse states, and left-going pulses propagate at the same velocity as right-going pulses.

I begin this section by discussing techniques for pro-

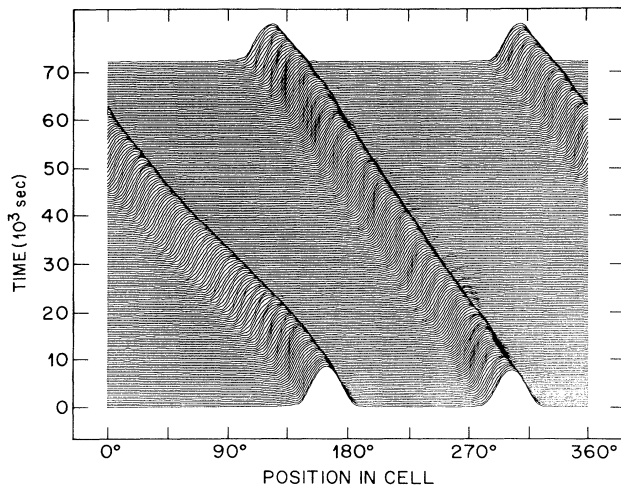


FIG. 4. Amplitude profiles of a state consisting of two pulses of left-going TW's, in a fluid with $\psi = -0.072$ in cell A, at $\bar{\epsilon} = 0.0090$. At each time step, one line of circular-camera data is demodulated in space at the measured mean wave number to produce a profile of the TW amplitude. Profiles at succeeding times are displayed in hidden-line format by shifting each profile vertically by an amount proportional to the elapsed time. In this data record, both pulses drift continuously to the left.

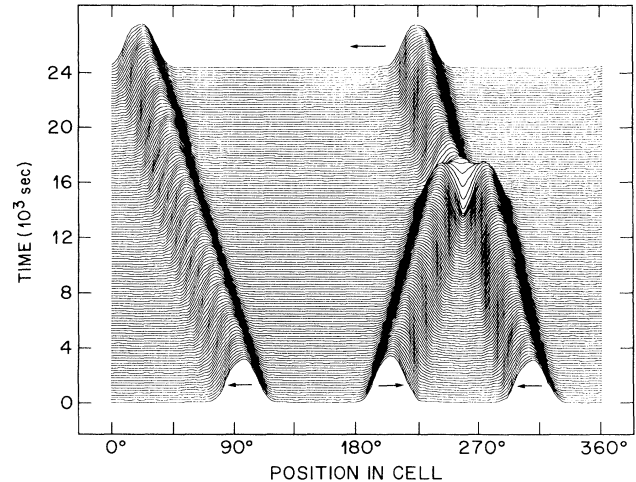


FIG. 5. Interaction of oppositely propagating pulses, in the same fluid and cell as in Fig. 4, but with $\bar{\epsilon} = 0.011$. Horizontal arrows underneath the pulses indicate the direction of propagation of the underlying TW. Because the pulses drift in the same direction as the TW, oppositely propagating pulses always meet, and only one of the two input pulses survives the resulting interaction. Under these conditions, the system always evolves into a state of copropagating pulses.

ducing stable states which consist of several copropagating pulses. There are several reasons why such states are useful. Multiple-pulse states produce data faster than single-pulse states. More importantly, spatial variations in v_{dr} can be sampled over the entire cell in less time using such a state than with a single-pulse state. Also, as shown in Ref. [7], pulses become unstable to destruction by convectively amplified fluctuations at a value of $\bar{\epsilon}$ which is inversely proportional to the length of the system. In a multiple-pulse state, as shown in Sec. VI, the relevant length for the growth of fluctuations is the spacing between pulses; thus such states remain stable to higher values of $\bar{\epsilon}$ than single-pulse states. This allows pulse-drift data to be taken at values of $\bar{\epsilon}$ at which single-pulse states are unstable. Finally, as discussed in Sec. VI, triple-pulse states attenuate fluctuations so much that a threshold for destabilization by an intrinsic mechanism can be reached.

Simply increasing $\bar{\epsilon}$ from below to above onset produces, after a long transient, a state which consists of several pulses—as many as six. However, this state usually consists of nearly equal numbers of left- and right-going pulses. Because the pulses drift in the direction of the underlying TW, pairs of counterpropagating pulses always approach each other and interact. As shown in Fig. 5, this interaction is fatal for one of the two input pulses, and it is not possible to predetermine which one survives. As a consequence, the most likely evolution of a spontaneously generated multiple-pulse state is for pulses to be removed from the system one by one, until a single pulse remains. A double-copropagating-pulse state

rarely occurs spontaneously, and I have never created a triple-copropagating-pulse state this way. Thus, simply jumping above onset is an unreliable way to produce multiple-copropagating-pulse states, and I have had to develop techniques for making such states.

There are several tools which can be exploited to add a pulse of a chosen direction and at a chosen location to an existing state. First, as described above and in Ref. [7], tapping on the end of one of the fill tubes injects a disturbance at each of the fill holes, and these grow into pulses above onset. Second, an existing pulse, properly located, can be used to absorb unwanted linear TW's [7]. Finally, if two quasilinear wave packets approach each other, nonlinear interactions will cause the amplitude of the weaker one to be suppressed, if the amplitude of the stronger one is large enough. Figure 6 illustrates the use of these effects to create a copropagating pulse at a location approximately diametrically opposite an existing pulse. Figure 6(a) shows the initial state, consisting of single right-going pulse at location 62° . Figure 6(b) shows the system just after disturbances have been injected at the fill holes, which are labeled 1 and 2. In Fig. 6(c), these disturbances have decomposed into linear wave packets: left- and right-going wave packets L_2 and R_2 originated at location 2, and right-going packet R_1 originated at location 1. The left-going wave packet L_1 has already been absorbed by the nonlinear pulse. Note that R_1 is about twice as strong as L_2 . During the time between Figs. 6(c) and 6(d), the Rayleigh number was manipulated near onset to keep the amplitude of R_1 high enough to have a nonlinear interaction with L_2 , but not

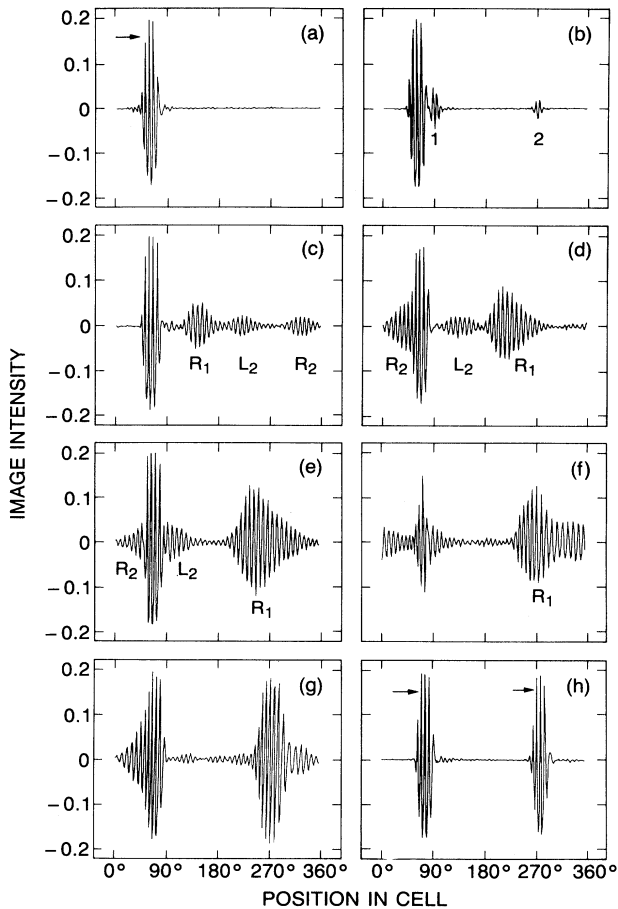


FIG. 6. Adding a second, right-going pulse to a single-pulse state in cell *C*, at $\psi = -0.123$. Linear wave packets are identified with the symbols L_1 , R_2 , etc., in which the letters refer to the propagation direction of the TW, and the subscripts refer to the point of origin: point 1 is the fill hole at location 90° , and point 2 is the fill hole at location 270° . (a) Initial single right-going pulse at $\bar{\epsilon} = 0.0177$. (b) Time $t = 0$. Tapping the fill tube creates a strong disturbance at location 1 and a weaker disturbance at location 2. (c) Time $t = 196$ sec. After propagation at $\bar{\epsilon} = 0.0177$, the disturbances have decomposed into left- and right-going linear wave packets R_1 , L_2 , and R_2 . L_1 has been absorbed by the existing pulse. At this point, $\bar{\epsilon}$ is reduced to 0.0011 to limit the growth of the linear TW. (d) Time $t = 868$ sec. After the interaction between L_2 and R_1 , the former is reduced in relative amplitude, because of weakly nonlinear interactions with the latter. R_2 is already being absorbed by the initial pulse. At this time, $\bar{\epsilon}$ is reduced to 0.0008 to prevent L_2 from growing too large to be absorbed by the pulse and to prevent R_1 from prematurely evolving into a pulse. (e) Time $t = 1148$ sec. $\bar{\epsilon}$ is increased to 0.0331 to cause R_1 to evolve into a pulse near location 270° . (f) Time $t = 1428$ sec. With R_1 stopped and at high amplitude, $\bar{\epsilon}$ is reduced to 0.0023 to limit the amplitude of newly created linear TW's. (g) Time $t = 1708$ sec. Linear TW's are nearly gone, and R_1 has nearly evolved into its final form. (h) Time $t = 3108$ sec. Final state of two copropagating pulses, approximately 180° apart.

so high as to prematurely evolve into a nonlinear pulse. As a result, the ratio of the amplitudes of R_1 and L_2 is even greater after than their interaction [Fig. 6(d)] than before [Fig. 6(c)]. Because the amplitudes of R_2 and L_2 have been kept small, they are absorbed when they collide with the original pulse [Fig. 6(e)]. Now, with the three other linear wave packets essentially gone, manipulations of the Rayleigh number are used to turn R_1 into a nonlinear pulse when it reaches the desired location. Just prior to Fig. 6(e), the Rayleigh number is increased to $\epsilon = 0.0331$. This causes R_1 to slow down and grow up into a pulse [Figs. 6(e)–6(g)]. During this evolution, R_1 emits strong, right-going linear TW's—these are evident in Fig. 6(f). In order to keep their amplitude small enough to be absorbed by the original pulse, the Rayleigh number is turned down to near onset at about the time of Fig. 6(f). The absorption of the remaining linear TW leaves a final state of two copropagating pulses, approximately 180° apart [Fig. 6(h)].

The procedure used in Fig. 6 can easily be extended to create a state of three copropagating pulses which are approximately equally spaced. The Rayleigh-number increase which turns R_1 into a pulse can be delayed, so that the final pulse stops near location 320° , approximately 120° away from the original pulse. Subsequently tapping on the fill tube then produces only wave packets R_1 and L_2 , because R_2 is immediately absorbed by the new pulse. The suppression of L_2 and the production of a right-going from R_1 then proceed essentially as above, with slight changes in timing. In Fig. 7, a third copropagating pulse is added to a preexisting two-pulse state by tapping

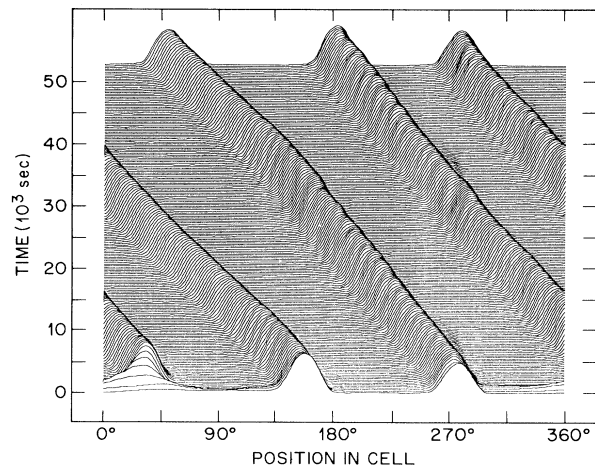


FIG. 7. A hidden-line plot of demodulated spatial amplitude profiles as functions of time shows the addition of a third, left-going pulse to a double-pulse state in cell *A*, at $\psi = -0.072$. In this case, with $\bar{\epsilon}$ held fixed at 0.0093, the fill tube is tapped as the two existing pulses move past locations 156° and 278° . The right-going wave packet originating at location 90° and the left-going wave packet originating at location 270° are immediately absorbed. The other two linear wave packets collide at location 34° ; since the left-going wave packet originating at 90° is the stronger of the two, a left-going pulse results.

on the fill tube as the original two pulses move into positions where they will rapidly absorb two of the injected wave packets. The larger amplitude of the left-going wave packet originating at location 90° causes it to suppress the right-going wave packet originating at 270° , resulting in the production of a third left-going pulse.

There are two other tools which have been used to facilitate these manipulations. The first is local heating, which is accomplished by applying a voltage to one or several of the small resistors arrayed around the lower edge of the bottom plate of cell *C*. Because (as shown below) both the drift velocity of a TW pulse and the growth rate of a linear wave packet depend on $\epsilon(x)$, an added local "hot spot" can be used to move an existing pulse to a new location, as well as to selectively enhance the growth of one or two linear wave packets over that of others. By adding and moving such local point sources of heat on the bottom plate, I have been able to create pairs of both counterpropagating and diametrically opposite copropagating pulses directly from the conducting state. Both processes take about an hour. Second, I have learned how to launch pulses from either of the fill tubes without exciting a disturbance at the other. This reduces the need to use pulses or quasilinear wave packets to absorb unwanted linear TW's.

With a suitably prepared state of pulses, the dependence of drift velocity on ϵ can be measured. I begin this measurement by acquiring circular-camera data at regular time intervals. At each time step, the amplitude profile is computed by demodulating in space at the mean measured wave number, and the position of each pulse is determined by computing the first moment of its amplitude profile. Differentiating in time gives the drift velocity v_{dr} as a function of spatial position x . v_{dr} is scaled by κ/d , where κ is the thermal diffusivity of the fluid and d is the cell height. Figure 8 shows the spatial dependence of $v_{dr}(x, \bar{\epsilon})$ measured using left-going pulses in cell *A* for $\psi = -0.072$ at several different values of $\bar{\epsilon}$. $v_{dr} < 0$ for left-going pulses, but I will consider only the absolute value of v_{dr} in what follows. Figure 8 shows that the magnitude of the average drift velocity increases with $\bar{\epsilon}$. Aside from this, the spatial structure of $v_{dr}(x, \bar{\epsilon})$ is reproducible from run to run, and from pulse to pulse in a given run. As shown below, this is just because $v_{dr}(x, \bar{\epsilon})$ is sensitive to the local value of $\epsilon(x)$.

For $\psi = -0.072$, v_{dr} was measured as a function of position in 19 runs at different values of $\bar{\epsilon}$, yielding 6445 separate measurements of $v_{dr}(x, \bar{\epsilon})$. Figure 9 shows the spatially averaged drift velocity $\bar{v}_{dr}(\bar{\epsilon})$ vs $\bar{\epsilon}$ for these 19 runs. The error bars in Fig. 9 are dominated by the spatial variation of v_{dr} . The drift velocity vanishes near onset and increases roughly linearly with $\bar{\epsilon}$. To within the error bars, multiple-pulse states exhibit the same drift velocity as single-pulse states. At this separation ratio, pulses lose stability and vanish when $\epsilon(x)$ is reduced below $\epsilon_2 = -0.001 \pm 0.002$.

From the 6445 measurements of $v_{dr}(x, \bar{\epsilon})$, both the intrinsic dependence of the drift velocity on Rayleigh number $v_{dr}(\epsilon)$ and the spatial dependence $\epsilon(x)$ can be extracted. For this purpose, I have developed an iterative pro-

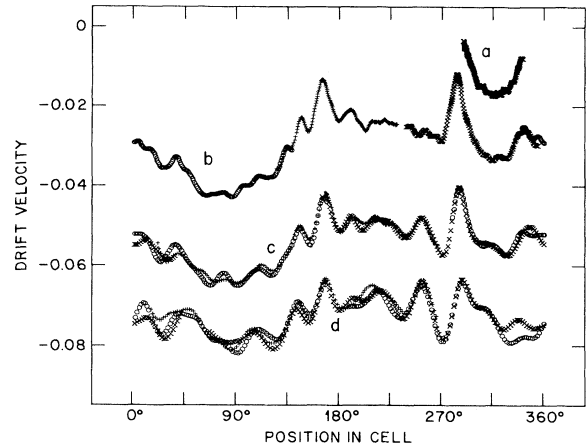


FIG. 8. Drift velocity v_{dr} vs spatial position in cell *A* for several different left-going pulses, at $\psi = -0.072$. (a) Single-pulse state $\bar{\epsilon} = 0.0027$. (b) Triple-pulse state $\bar{\epsilon} = 0.0065$. The three pulses are represented by different symbols: +, \circ , and \times . (c) Triple-pulse state $\bar{\epsilon} = 0.012$. (d) Triple-pulse state $\bar{\epsilon} = 0.017$. The absolute value of the average drift velocity increases with increasing $\bar{\epsilon}$. The spatial structure of $v_{dr}(x)$ is reproducible from run to run as well as from pulse to pulse in a single run.

cedure which begins with a postulated inverse dependence $\epsilon(v_{dr})$. In the present case, I start by fitting the data in Fig. 9 to a straight line, although, as will shortly become clear, a parabola would be a better choice. Then, for each of the 6445 measurements of $v_{dr}(x, \bar{\epsilon})$, the fitted $\epsilon(v_{dr})$ is used to calculate the stress-parameter nonuniformity $\delta\epsilon(x) = \epsilon(v_{dr}(x, \bar{\epsilon})) - \bar{\epsilon}$. If the dependence $v_{dr}(\epsilon)$ is close to linear over the range of variations in each individual run, then $\delta\epsilon(x)$ should match the curves in Fig. 2(c). The results for $\delta\epsilon(x)$ are binned in space and averaged to produce the full curve in Fig. 10; the error bar is twice

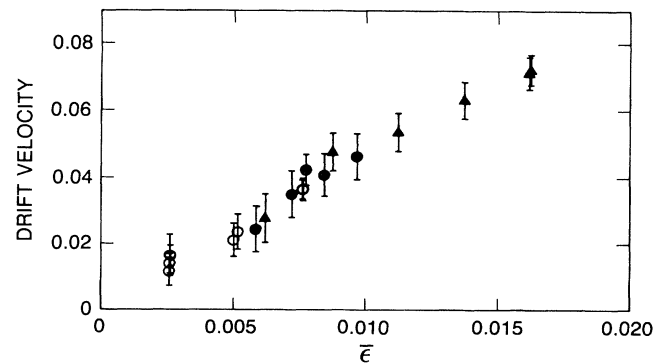


FIG. 9. Average drift velocity vs $\bar{\epsilon}$ for $\psi = -0.072$. Each symbol represents the spatially averaged value \bar{v}_{dr} in a run like those in Fig. 8, plotted at the value of $\bar{\epsilon}$ for that run. The error bars represent twice the standard deviation of the spatial variation of v_{dr} for each point. Open circles, single-pulse states; solid circles, double-pulse states; triangles, triple-pulse states.

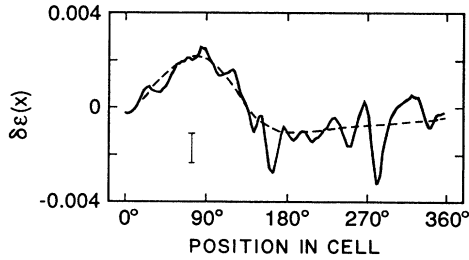


FIG. 10. Full curve: binned and averaged values of the stress-parameter nonuniformity $\delta\epsilon(x)$ for cell *A*, as deduced from pulse-velocity data in Figs. 8 and 9. The error bar represents twice the average of the standard deviations in each of the bins. Dashed curve: average of the two curves $\epsilon_{L,R}(x)$ shown in Fig. 2 (c), shifted to the right by 21° or $4.4d$.

the average of the standard deviations in the individual bins. For comparison, the dashed curve is the average of the two estimates $\epsilon_{L,R}(x)$ shown in Fig. 2(c). The pulse-velocity result matches the low-spatial-frequency component of the linear-TW result quite well. For the best agreement between the two measured profiles, I have shifted the linear-TW curve to the right by 21° , which corresponds to 4.4 times the cell height, or approximately one pulse width. Thus it appears that $v_{dr}(x)$ depends on the value of $\epsilon(x)$ measured at its leading edge. A more precise measurement of the shift between the pulse center and the $\epsilon(x)$ profile, made by studying the drift of a pulse through a peak in $\epsilon(x)$ at a known location, will be described in the following article [19].

It is worth pausing to note that measurements of pulse drift have yielded an extremely useful assessment of the uniformity of the experimental cell which is complementary to that obtained by stabilizing linear TW states. The results in Fig. 2(c) depend on the values of the parameters in Eqs. (1) and (2) and explicitly rely on a theoretical model which cannot describe fast spatial variations. In contrast, the pulse-velocity result in Fig. 10 relies on no theory and is self-calibrating. The true spatial resolution of this measurement depends on noise, properties of the optical system, and on the nature of the interaction of the pulse with inhomogeneities, and these are subjects of ongoing investigation. While it is encouraging that two results based on different dynamical states agree, the pulse-velocity measurement is much easier to perform and is more reliable and accurate. Investigations made since the preliminary report of this work [12] have revealed that the sharp dips at locations 160° and 280° in the pulse-velocity measurement of $\epsilon(x)$ were caused by two tiny droplets of an oily liquid which slowly grew over the month during which the measurements were made. These therefore had a time-dependent effect on these measurements, leading to the rather large error bar in Fig. 10. By contrast, the linear-TW results in Fig. 2 were made some time previous to the first observation of the droplets and would have an unknown sensitivity to them.

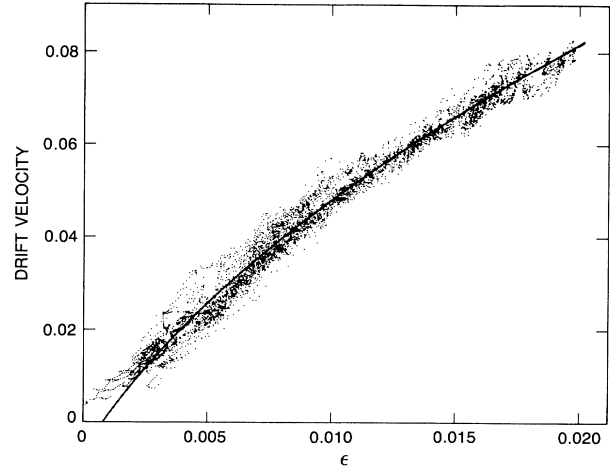


FIG. 11. Pulse drift velocity v_{dr} as a function of stress parameter ϵ , for $\psi = -0.072$. Each data point represents an individual measurement of $v_{dr}(x, \bar{\epsilon})$ and is plotted at the corresponding calculated value of $\epsilon(x, \bar{\epsilon})$. The smooth curve is a square-root fit to the data. No measurements were made for $\bar{\epsilon} \lesssim 0$, although it appeared that pulses lose stability near $\epsilon = 0$ at this value of ψ .

These droplets were traced to the cell gaskets and were eliminated by soaking them in ethanol for a week before assembling cells *B* and *C*.

Using the averaged spatial dependence of $\delta\epsilon(x)$ in Fig.

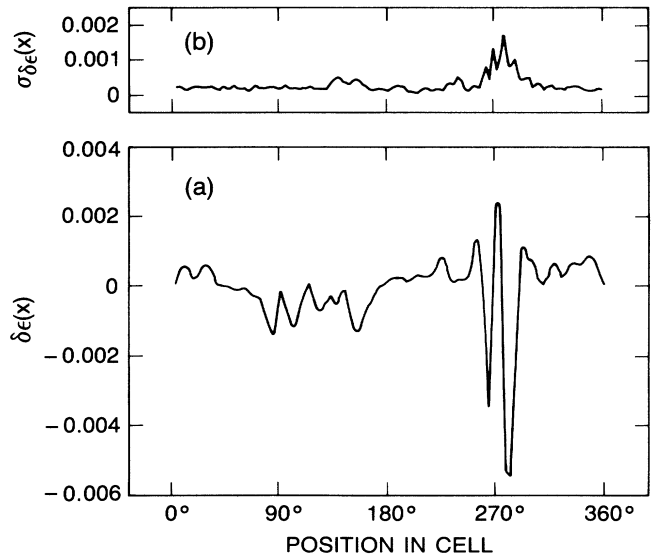


FIG. 12. (a) Local stress-parameter nonuniformity $\delta\epsilon(x)$ for cell *B*, deduced from measurements using double left-going pulses and single-right-going pulses at $\psi = -0.101$. A sharp feature is observed at location 270° . The rest of the cell is uniform to $\pm 0.1\%$. (b) Standard deviation $\sigma_{\delta\epsilon(x)}$ of the measurements in (a). Outside the region of the sharp feature, the small standard deviation indicates that $\delta\epsilon(x)$ was quite stable during the course of the experiments.

TABLE II. Parameters of fits to pulse drift velocities

ψ	v_0	a	ϵ_0	rms error	ϵ_2^a
-0.072	0.051	0.890	0.002 48	0.0027	-0.001±0.002
-0.101	0.050	0.899	0.006 24	0.0013	-0.0042±0.0004
-0.123	0.058	0.931	0.013 97	0.0018	-0.0118±0.0004

^aWhen the local value $\epsilon(x)$ is reduced below the lower stability limit ϵ_2 , pulses lose stability and disappear.

10, the true local stress parameter $\epsilon(x, \bar{\epsilon}) = \bar{\epsilon} + \delta\epsilon(x)$ can be calculated for each of the 6445 measurements of $v_{dr}(x, \bar{\epsilon})$, thus removing the dependence on the spatial coordinate x . The resulting data for $v_{dr}(\epsilon)$ are plotted in Fig. 11. This graph is equivalent to that in Fig. 9, except that, with the spatial dependence removed, the average standard deviation of the points in a narrow interval in ϵ is about 2 times smaller than that corresponding to the error bars in Fig. 9. The smooth curve in Fig. 11 shows a fitted function of the form $v_{dr}(\epsilon) = -v_0 + a(\epsilon + \epsilon_0)^{1/2}$. With this fit, the iterative procedure can be restarted, resulting in a further slight reduction in scatter. With the fit parameters in Table II, this functional form fits the data with a rms error of 0.0027. Other functional forms, such as a straight line, give a noticeably worse fit. This is more evident in the data presented below.

Cell *B* was constructed using a different bottom plate and spacer than cell *A*. The stress-parameter profile $\delta\epsilon(x)$ measured using left-going pulses in cell *B* with $\psi = -0.101$ is shown in Fig. 12. Somewhat surprisingly, a sharp feature is observed near location 270° . As noted above, this defect made it impossible to stabilize a single-mode linear TW state, and this cell can be regarded as useless for accurate observations of uniform, cell-filling

convective states. However, the rest of the cell is quite uniform, and, since the drift of a localized pulse is sensitive only to the value of $\epsilon(x)$ at its leading edge, it appears quite reasonable simply to discard the data obtained near the sharp features in Fig. 11. The resulting measurements of $v_{dr}(\epsilon)$, shown in Fig. 13, indeed exhibit much less scatter than those in Fig. 11, and this is mostly due to the fact that $\epsilon(x)$ was more stable in time than during the previous experiments. Using the parameters in Table II, the square-root form proposed above fits the positive-velocity data with a rms error of only 0.0013. It should be noted in Fig. 13 that the pulse velocity remains approximately zero over a tiny range in ϵ below the value at which this functional form passes through zero. The fit to the square-root form excluded these data. When $\epsilon(x)$ is reduced from -0.0036 to -0.0047 , the pulse loses stability and vanishes.

Cell *C* was made simply by disassembling cell *B*, cleaning it, reseating the gasket seal, and reassembling. A pre-

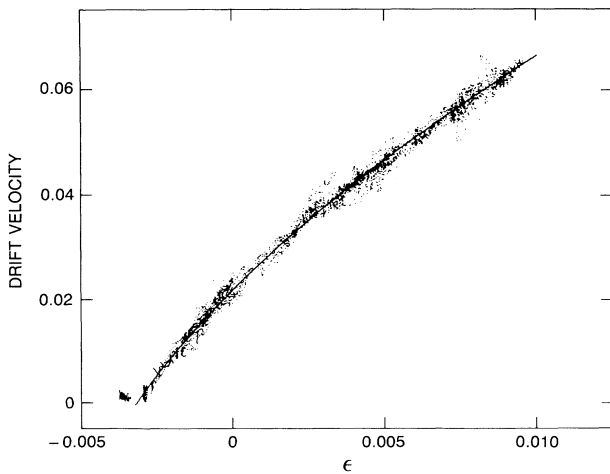


FIG. 13. Pulse drift velocity v_{dr} as a function of stress parameter ϵ , for $\psi = -0.101$. The individual data points were obtained as in Fig. 11, using a double-left-pulse state and a single-right-pulse state. The smooth curve is a fit using the same square-root functional form.

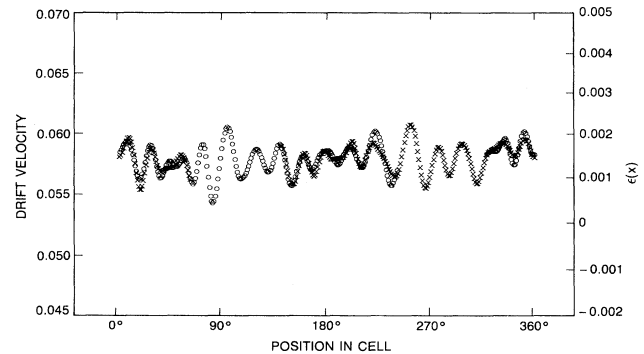


FIG. 14. Drift velocity v_{dr} measured as a function of spatial position at $\bar{\epsilon} = 0.0016$ using a state of two right-going pulses in a fluid with $\psi = -0.123$ in cell *C*. As a result of careful trimming of the heat applied to the lower plate of the cell, the drift-velocity profile is extremely uniform, except for wiggles which appear to be the residual effects of optical distortions. These measurements are calibrated against ϵ on the right-hand axis of the graph, using the fit of $v_{dr}(\epsilon)$ in Fig. 15. Without any smoothing of the wiggles, averaging the entire $\epsilon(x)$ profile yields a standard deviation of 3.2×10^{-4} . Convoluting this $\epsilon(x)$ profile with the pulse-amplitude profile in Fig. 16(a), as a guess of the fluctuation level truly felt by the pulse, reduces this to 1.0×10^{-4} . This value drifted back up to 1.9×10^{-4} after a week of experiments.

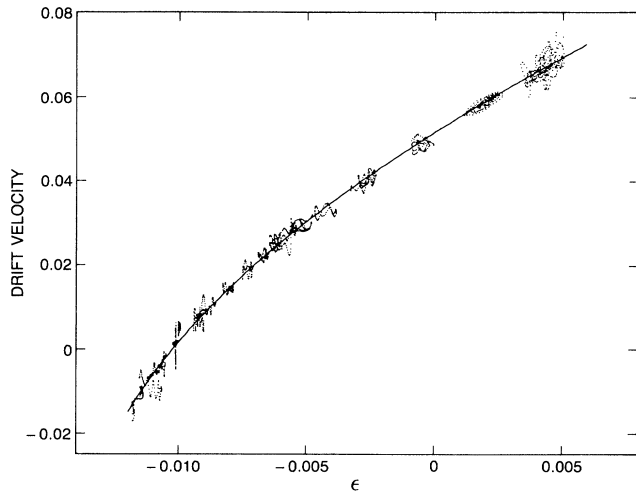


FIG. 15. Pulse drift velocity v_{dr} as a function of stress parameter ϵ , for $\psi = -0.123$. Most of the data points below $\epsilon = -0.009$ were obtained using a single right-going pulse in the original, nonuniform cell. The rest of the data come from measurements on a double-right-going-pulse state made after the cell uniformity was improved to the level in Fig. 14. The two data runs agree and are well fit by the square-root functional form (solid curve). There is no evidence of pinning at zero velocity.

liminary series of experiments with $\psi = -0.123$, made as above, produced a smooth $\delta\epsilon(x)$ profile of peak-to-peak amplitude 0.005, demonstrating that the sharp feature in $\delta\epsilon(x)$ in cell *B* had been removed. About 20% of this nonuniformity can be attributed to the measured nonuniformities in cell geometry. These runs also yielded the parameters of the square-root dependence of $v_{dr}(\epsilon)$. Then, using techniques described in Ref. [19], additional local heating of the bottom plate was adjusted to yield a uniform pulse-velocity profile. As shown in Fig. 14, a spatial uniformity in $\delta\epsilon(x)$ of parts in 10^4 was achieved. With this level of uniformity, it is no longer necessary to amass large amounts of data for accurate measurement of $\epsilon(x)$. Rather, two rapid scans in $\bar{\epsilon}$ were performed, and the measured drift velocity is plotted versus ϵ in Fig. 15. In analyzing these data, two full measurements of $\epsilon(x)$ as in Fig. 14, were made before and after the data scans, so that the iterative data-analysis procedure could be extended to allow ϵ to be interpolated both in time and in space for each experimental point in Fig. 15. However, $\epsilon(x, t)$ was so stable and uniform that this additional correction had little effect on the quality of the data. These data continue to be well fit by the square-root dependence $v_{dr}(\epsilon)$. Note also in Fig. 15 that a substantial region of negative drift velocity is seen at this value of ψ , and that there is no evidence of pinning at zero velocity. The laboratory frame is not sensed by these pulses.

V. PULSE SHAPE

In Ref. 2, the shapes of motionless traveling-wave pulses were analyzed by fitting raw shadowgraph data to

a function with a spatially symmetric amplitude profile which is a stationary solution of the lowest-order subcritical Ginzburg-Landau equation. Reasonably good fits were obtained, and the principal parametric evolution was a weak increase of pulse width with ϵ . The fit function exhibits a strong spatial gradient in wave number, and this also gave a good fit to the data. In addition, these experiments established that pulse shapes are the same in annular and rectangular containers. These fits have recently been repeated at several different separation ratios by the authors of Ref. [20]. Their pulses appear to be slightly longer than those in Ref. [2], but otherwise, the reported weak dependence of pulse width on ψ and ϵ is consistent with the earlier measurements.

The technique of fitting data to a chosen function has the disadvantage that fits may be possible even if an incorrect function is used. Extraction of wave amplitudes by complex demodulation [15] is a complementary technique in which the correct pulse shape appears as an out-

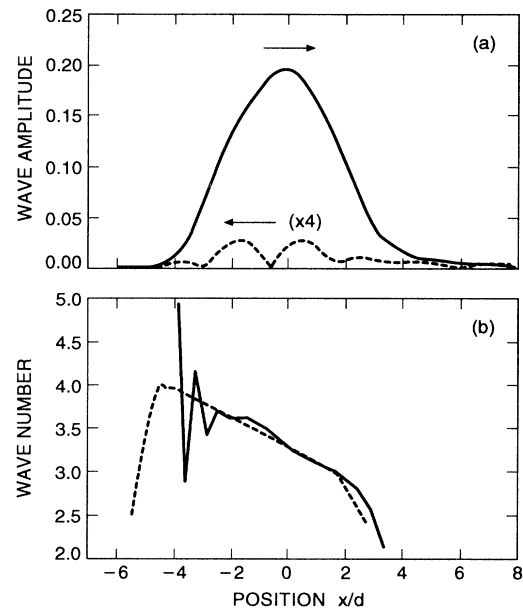


FIG. 16. (a) Right-wave (full curve) and left-wave (dashed curve) amplitude profiles computed for a right-going pulse at a local value $\epsilon(x) = -0.0084$ in cell *C* with $\psi = -0.123$. Here, the spatial position x is scaled by the cell height d and is shifted so that the centroid of the main pulse is at $x = 0$. The right-wave component exhibits a reproducible leading-edge shoulder. The main body of the pulse exhibits slight asymmetry which is not reproducible. The left-wave component has a very low amplitude and exhibits a phase defect. This computation was performed using a demodulator with very wide spatial and temporal bandwidths; it was verified that further increases in bandwidth did not result in any systematic change in pulse shape. (b) The solid curve shows the wave number of the right-going component of the pulse in (a). A strong gradient and a steep drop at the leading edge of the pulse are reproducible features. The dashed curve is the wave-number profile exhibited by the numerical pulse computed in Ref. [11].

put rather than as an input. A potential disadvantage of this technique is that it requires bandpass filtering, and this may cause distortions in the output pulse shape if the data exhibit a strong variation in wave number and/or frequency. However, because of the low noise level in these experiments, the demodulator bandwidth can be wide enough to encompass the entire range of wave number and frequency variation in the data and still produce a clean output.

Pulse shapes were studied in detail as a function of ϵ for $\psi = -0.123$. Figure 16 shows the computed amplitude and wave-number profiles for a right-going pulse at $\epsilon = -0.0084$. The right-wave component in Fig. 16(a) consists of a slightly asymmetric pulse with a noticeable leading-edge shoulder. The weak asymmetry in the main body of the pulse is not reproducible, and I suspect that its cause is residual optical distortions. However, the shoulder is a reproducible feature of all the traveling-wave pulses I have studied. This particular pulse was chosen for display because its chosen for display because its amplitude profile is virtually indistinguishable from the pulse which was numerically computed for $\epsilon = 0.008$ and $\psi = -0.08$ in Fig. 4 of Ref. [11]. The main body of the pulse can also be reasonably well fit using the functional form cited in Refs. [2] and [20]. The fit parameters obtained are similar to those found by those authors, but the leading-edge shoulder is a feature not accounted for by the symmetric amplitude profile of that function.

The amplitude profile of the counterpropagating-wave component is shown by the dashed curve in Fig. 16(a). The sharp amplitude null seen at $x/d = -0.6$ is due to a phase defect which appears as a singularity in the corresponding wave-number profile at the same spatial point (not shown). Weak, noisy, defected counterpropagating-wave components are the rule in these experiments and are also evident in pulses in rectangular cells [cf. Fig. 2(b), Ref. [21)]. The present results lead to the somewhat puzzling deduction that reflections from an end wall cannot be their cause.

The solid curve in Fig. 16(b) shows the wave-number profile computed for the right-wave component of this pulse. The principal reproducible features of this profile are its steep spatial gradient and the sharp drop in wave number at the leading edge of the pulse. If the demodulator bandwidth used in this computation is decreased for noise reduction, the erratic trailing edge of the profile tends to smooth out and turn upward, imparting a sigmoidal shape. However, it is not clear that this is the proper way to reduce the noise in this profile. The gradient and center wave number of the wave-number profile are quite similar to those exhibited by the functional form used to fit pulse shapes in Refs. [2] and [20]. However, the overall shape of the wave-number profile is almost perfectly matched by that of the numerically computed pulse in Ref. [11] (dashed curve). The slight difference between the numerical and experimental wave numbers at the very leading edge of the pulse may be due to the fact that the numerical profile was computed by counting zero crossings rather than by demodulation.

In light of the observation by Deissler and Brand [10] that the nonlinear gradient terms which introduce a pulse

drift into the solutions of the complex Ginzburg-Landau equation also cause an asymmetric pulse shape, it may be of significance to understand the evolution of the experimental pulse shape with ϵ . I have chosen to parametrize this dependence by computing the first few moments of the pulse amplitude profile. For a profile $A(x)$, whose n th moment I_n is

$$I_n = \int_{-\infty}^{\infty} x^n A(x - x_0) dx, \quad (4a)$$

where x_0 is set so that $I_1 = 0$, I compute the n th moment length L_n :

$$L_n = (I_n / I_0)^{1/n}. \quad (4b)$$

The lengths L_n are scaled in units of the cell height. The

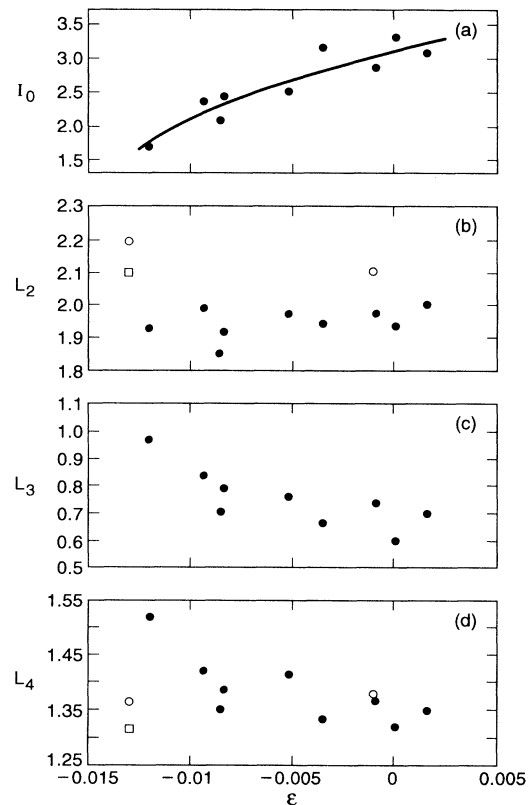


FIG. 17. Amplitude and first three nonvanishing moment lengths computed vs ϵ for experimental and theoretical pulse amplitude profiles. (a) Pulse amplitude I_0 . (b) Pulse width L_2 . (c) Asymmetry length L_3 . (d) Fourth-moment length L_4 . The solid circles represent experimental pulses at $\psi = -0.123$. The scatter in the data appears to be due to the unreproducible asymmetry noted above in the pulse in Fig. 16(a). The smooth curve in (a) is a fit to the functional form $I_0 = b + a(\epsilon + \epsilon_0)^{1/2}$, with the value $\epsilon_0 = 0.01397$ taken from Table II. The open squares plotted at $\epsilon = -0.013$ are computed for a Gaussian of FWHM 5.0. The open circles at $\epsilon = -0.013$ and -0.001 are computed using the function and fit parameters in Fig. 4 of Ref. [2].

closed circles in Figs. 17(a)–17(d) show the dependence on ϵ of the zeroth moment and the first three nonzero moment lengths of experimental pulses at $\psi = -0.123$. Not surprisingly, the pulse amplitude I_0 increases with ϵ . The smooth curve in Fig. 17(a) is a fit to the square-root dependence followed by the drift velocity, with ϵ_0 fixed at the value $\epsilon_0 = 0.01397$ found for this value of ψ . The pulse width L_2 increases weakly with ϵ , with a slope that is consistent with those reported in Refs. [2] and [20]. Interestingly, the asymmetry length L_3 shows a pronounced decrease with ϵ . A weaker decrease is exhibited by L_4 . The open symbols in Figs. 17(b) and 17(d) show the moment lengths computed for three symmetric pulse shapes: a Gaussian of full width at half maximum (FWHM) 5.0 (open square plotted at $\epsilon = -0.013$) and the Ginzburg-Landau solutions fitted at $\epsilon = -0.013$ (FWHM equal to 5.4) and -0.001 (FWHM equal to 5.0) in Fig. 4 of Ref. [2] (open circles). The experimental L_2 can be matched by altering the fit parameters of the latter function, but to simultaneously match L_4 requires unreasonable parameter values. Of course, odd moments vanish for these symmetric functions.

VI. FLUCTUATION SUPPRESSION AND INTRINSIC PULSE DESTABILIZATION

Several references have been made in this paper to suppression of linear TW fluctuations by pulses. These statements are based on the work described in Ref. [7], in which it was found that small-amplitude linear TW's are absorbed by pulses, while large-amplitude linear TW's destroy them. Because small fluctuations are always present in this system, and because linear TW's are convectively unstable above $\bar{\epsilon} = 0$, we argued that these observations imply that, in a system of length Γ , pulses should be stable against destruction by fluctuations up to a value $\epsilon_f \propto 1/\Gamma$. This in turn implies that, in an annular container, a state of N equally spaced pulses should be stable up to $\bar{\epsilon} \propto N$. This is fluctuation suppression.

Figures 18 and 19 show that this argument is correct. Figure 18 illustrates a single-pulse state at $\bar{\epsilon} = 0.0081$, with $\psi = -0.072$. At this value of $\bar{\epsilon}$, spontaneously generated linear TW's are convectively amplified into a coherent wave packet which becomes visible at the end of the data record. Judging from the large amplitude of these TW's, it appears that a small further increase in $\bar{\epsilon}$ would lead to the destruction of the pulse. The length over which linear TW's are convectively amplified in this state is just the system length minus the pulse width, or 66 times the cell height.

For a double-pulse state, TW fluctuations become visible only at higher $\bar{\epsilon}$. As shown in Fig. 19, convectively amplified fluctuations first reach the level shown in Fig. 18 only at $\bar{\epsilon} = 0.0121$. In this run, the two quiescent regions were of different size, and the longer region had a length of 40 times the height of the cell. The ratio of the values of $\bar{\epsilon}$ in Figs. 18 and 19 is indeed inversely proportional to the ratio of the lengths of the largest nonconvecting regions in the cell, to within 10%. This supports the argument in the preceding paragraph. Quantitative observations and modeling of this kind of convective

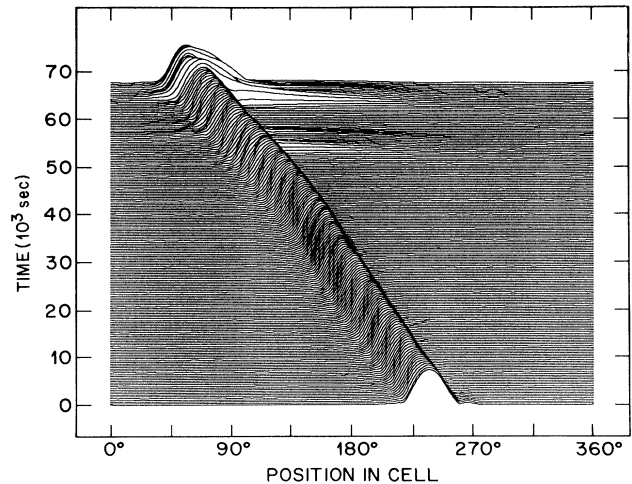


FIG. 18. Single-left-pulse state in cell A with $\psi = -0.072$ and $\bar{\epsilon} = 0.0081$. Over the course of the run, convectively amplified TW fluctuations produce a strong, coherent wave packet which becomes visible at the end of the data record. The dimensionless length of the nonconvecting region in this run is 66.

amplification of TW fluctuations have recently been reported by Schöpf and Rehberg and Rehberg *et al.* [22].

These numbers imply that a state consisting of three equally spaced pulses should exhibit TW fluctuations of substantial amplitude only for $\bar{\epsilon} \sim 0.03$. However, such high values have never been reached in these experiments, because, as shown in Figs. 20 and 21, pulses lose stability via a different mechanism well before this. Figure 20 shows the evolution of a triple-pulse state at high $\bar{\epsilon}$. At $t = 5040$ sec, just as the center of one of the

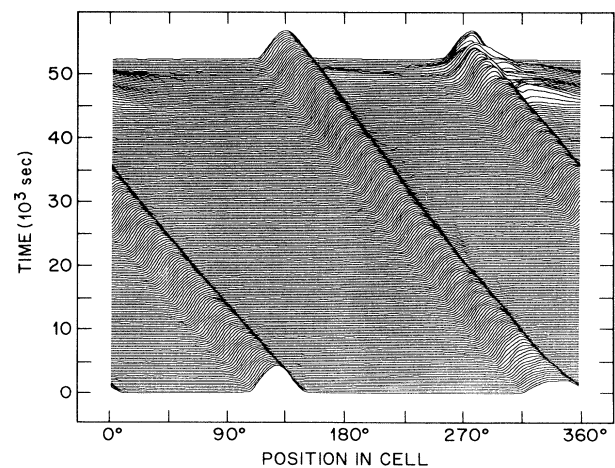


FIG. 19. Double-left-pulse state in cell A with $\psi = -0.072$ and $\bar{\epsilon} = 0.0121$. As in Fig. 18, a convectively amplified wave packet becomes visible at the end of the run. The dimensionless length of the larger nonconvecting region in this run is 40.

pulses—the one at position 110° at the beginning of the run—moves into the region of positive $\delta\epsilon(x)$ shown in Fig. 10, $\bar{\epsilon}$ is increased from 0.0172 to 0.0185. Because of the drift and the jump in $\bar{\epsilon}$, the local value of $\epsilon(x)$ at the center of this pulse increases from 0.017 to 0.020. In response, the TW's in the pulse begin to slow down, and then the pulse envelope begins to expand. At $t=21\,000$ sec, when the velocity of the underlying TW has slowed to a value ~ 5.2 times lower than its value at the beginning of the run, $\bar{\epsilon}$ is reduced to 0.0091. The broadened pulse of slow TW then drifts through the region of elevated $\delta\epsilon(x)$, reverting to its original form many hours later.

The pulse that undergoes the destabilization just de-

scribed appears to do so because it passes through a region of space-time where $\epsilon(x)$ exceeds a threshold $\epsilon_1=0.019\pm 0.001$. What about the other two pulses? Because of the timing of the changes in $\bar{\epsilon}$ and the spatial structure of $\delta\epsilon(x)$, the pulse that was initially at location 340° was never exposed to values of values $\epsilon(x)$ greater than 0.016, and the last pulse, while briefly drifting through a region in which $\epsilon(x)>0.019$, appears not to have enough time to go unstable. Thus the only function of the other two pulses is to absorb fluctuations which would otherwise destroy the broadened pulse. Thus the destabilization of that pulse appears to be caused by an intrinsic mechanism with a high threshold. This mechanism is hysteretic, as indicated by the persistence of the broadened pulse when $\bar{\epsilon}$ is reduced well below ϵ_1 . A

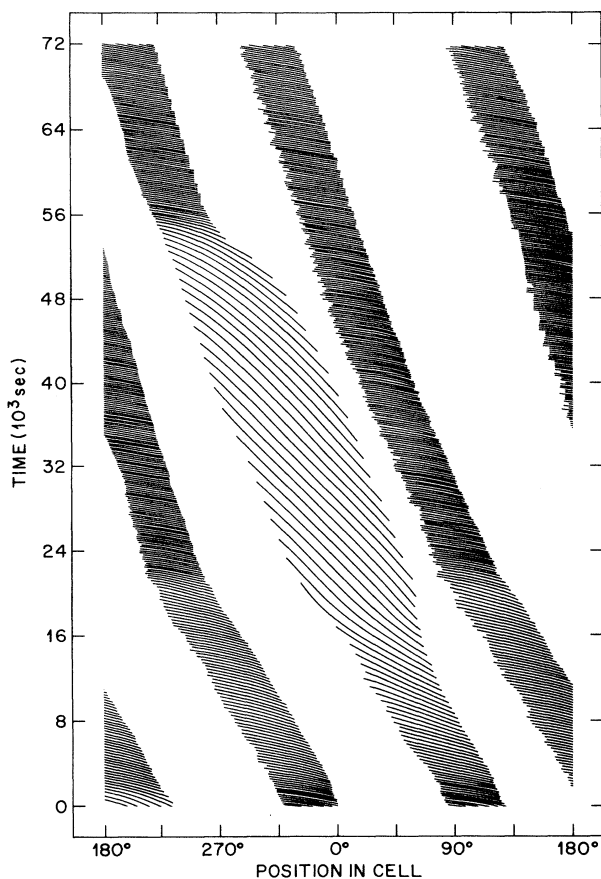


FIG. 20. Evolution of a triple-pulse state in cell *A* with $\psi=-0.072$, at high $\bar{\epsilon}$. In this space-time plot, smooth curves connect points of equal phase, allowing the propagation of the underlying TW to be seen directly. The horizontal axis has been shifted by 180° for clarity. Initially, $\bar{\epsilon}=0.0091$. At $t=2220$ sec, $\bar{\epsilon}$ is increased to 0.0172, and again to 0.0185 at $t=5040$ sec. $\bar{\epsilon}$ remains at this value until $t=21\,000$ sec, at which time it is reset to 0.0091. Because of these manipulations, and because of the slightly elevated value of $\epsilon(x)$ in the region between 0° and 130° , one pulse drifts through a region of elevated $\epsilon(x)$ and undergoes a destabilization in which the pulse envelope expands into the rest of the system and the underlying TW's slow down drastically. The other two pulses retain their original forms and serve only to absorb TW fluctuations.

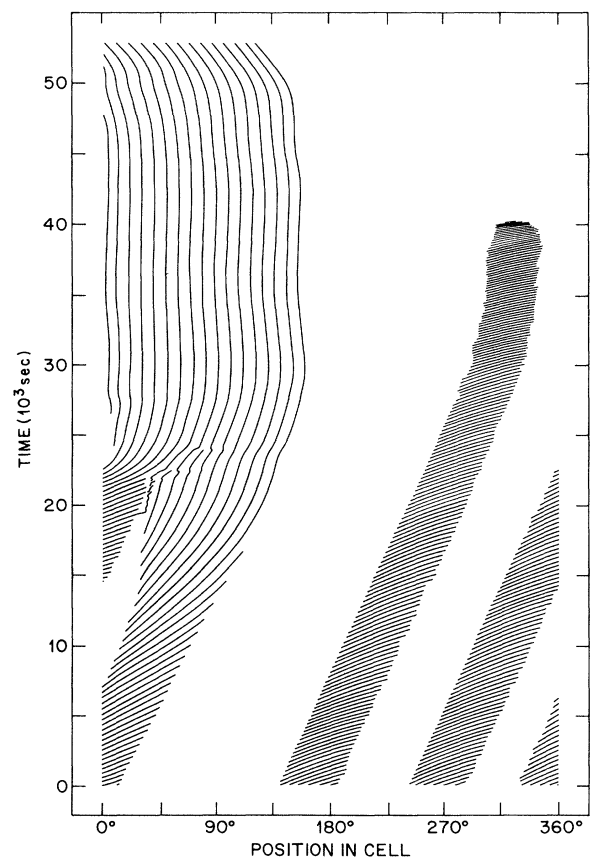


FIG. 21. Another intrinsic destabilization at $\psi=-0.072$ in cell *A*. Initially, $\bar{\epsilon}$ is estimated to be 0.018, and one of the three pulses begins to exhibit a deceleration of its TW and broadening of its amplitude profile. Following a collision with a drifting pulse of fast TW's, $\bar{\epsilon}$ is reduced to 0.0150, at time $t=25\,260$ sec. This leaves the system with a wide confined state of nearly motionless rolls and a slowly drifting pulse. The confined state of essentially stationary rolls persists even after $\bar{\epsilon}$ is reduced to 0.0070 at time $t=29\,660$ sec. Finally, the confined region is induced to decay, long after $\bar{\epsilon}$ is reduced to -0.0064 at $t=38\,590$ sec.

slightly nonuniform cell and the suppression of fluctuations have been crucial in making this observation.

Figure 21 shows another intrinsic destabilization of one of three right-going pulses. Unfortunately, the initial value of $\bar{\epsilon}$ was not recorded for this run, but, judging from the behavior, I estimate that $\bar{\epsilon}=0.018$. Shortly after the beginning of the run, the pulse whose initial location is near 0° starts to go unstable in a manner very similar to that shown in Fig. 20. By the time $\bar{\epsilon}$ is reduced to 0.0150 (at $t=25\,260$ sec), the TW's in that pulse have slowed to almost zero velocity, and additional rolls have been added by the collision of one of the other two pulses. At $t=29\,660$ sec, $\bar{\epsilon}$ is reduced to 0.0070, and the result is a very broad confined state of *nearly stationary* rolls. The rest of the system is kept clear of TW fluctuations by the remaining pulse, which disappears when $\bar{\epsilon}$ is reduced to -0.0064 at time $t=38\,590$ sec. Ultimately, this causes the broad confined state of nearly motionless rolls to vanish as well.

The initial evolution of the destabilized pulse in Fig. 21 is similar to that in Fig. 20: decreasing TW velocity, followed by expansion of the amplitude profile into the rest of the system. Again, the broadened pulse appears to be hysteretic. In both cases, it seems likely that it is possible to find a band of $\bar{\epsilon}$ over which the broadened pulse is stable. In particular, at $\bar{\epsilon}=0.0070$, except for the leftover drifting pulse, it appears that the broad region of essentially stationary rolls in Fig. 21 was stable. Clearly, both the spatial extent of the destabilized pulse and the velocity of the underlying TW are sensitive functions of the history of the system.

VII. DISCUSSION

The initial results presented in this paper document the continued evolution of the control and perfection possible in the experimental study of convection in binary fluids. Using the techniques discussed in Sec. III and IV, it has been possible to precisely measure the experimental geometry and to control the principal stress parameter ϵ with stabilities of parts in 10^5 in time and of parts in 10^4 in space. The shadowgraph technique and the methods used for data analysis have also progressed so far that the fundamental excitations of the system—traveling waves—can be extracted and characterized with practically no noise or distortion. Thus, even with an extremely wide demodulator bandwidth, the right-wave amplitude profile in Fig. 16(a) has a signal-to-noise ratio of several hundred at its peak. With these and other advances in experimental technique, traveling-wave convection in an annular container has evolved into an extremely high-precision testing ground for understanding nonlinear pattern formation in one dimension.

Theoretical understanding of this system on the basis of the full Navier-Stokes equations is also quite advanced. The numerical calculations of Ref. [11] give an excellent qualitative accounting of the pulse amplitude and wave-number profiles seen in these experiments. Because of the differences in ψ and ϵ between the theory and the experiment, the nearly exact *quantitative* agreement in Fig. 16 is probably fortuitous. However, there seems little reason

to doubt that the theoretical calculations are essentially correct, and that quantitative agreement in the pulse shape will be obtained for computations and experiments performed at the same parameter values. This optimism is reinforced by the close agreement between parameter-matched numerical calculations and experiments on the confined states of arbitrary length seen at more negative separation ratio [23] that has been reported recently [24]. There remain small discrepancies among the pulse shapes reported here and in Refs. [2] and [20]—in particular, the pulses in those reports do not appear to exhibit the leading-edge shoulder seen in Fig. 16 and in the computations of Ref. [11]. The reason for this is not simply that the pulses in Refs. [2] and [20] are motionless. Motionless pulses in the present experiment (created by setting $\epsilon=-0.0101$ at $\psi=-0.123$) exhibit a pronounced asymmetry due to the shoulder—cf. Fig. 17(c). This suggests that the weak experimental imperfections which apparently pinned the pulses in Refs. [2] and [20] to zero velocity also had an effect on their shape.

Despite the apparently excellent theoretical accounting for the shape of drifting pulses, the parametric dependences of their drift velocity and stability, as well as their shape, still leave several quantitative issues for theory to resolve. First, the drift velocity increases monotonically in ϵ for fixed ψ and decreases monotonically in ψ for fixed ϵ . The latter dependence allows the value $v_{\text{dr}}=0.039$ (0.057) to be interpolated for the parameters of Ref. [11]: $\epsilon=0.0069$ (0.0115) and $\psi=-0.08$. Those numerical computations yield $v_{\text{dr}}=0.051$ (0.082) [25], quite reasonable agreement considering the uncertain effects of the narrow lateral dimension of the cell used in these experiments. Second, the pulse asymmetry, as measured by the moment length L_3 , decreases with ϵ at $\psi=-0.123$. Finally, the pulse loses stability when ϵ drops below a value ϵ_2 , which increases with ψ . While it seems quite likely that the computations of Ref. [11] can account for these measurements quantitatively, this has yet to be done explicitly.

Ginzburg-Landau-type models have become extremely popular for the theoretical description of pattern-forming systems. For the present system, such an equation is the direct result of an analysis of the Navier-Stokes equations which treats the convection as a small perturbation of the quiescent, conducting state seen just below onset [17]. One of the attractions of this system is that the coefficients in both the linear [16,17] and first nonlinear [26,27] terms of the Ginzburg-Landau equation have been accurately calculated and measured, and the resulting equations have been shown to correspond quite well to observed behavior in the weakly nonlinear case, i.e., at small negative ψ [27,28]. Thus, just as it was encouraging to find in Ref. [2] that experimental pulses could be well fit by a solution of the lowest-order subcritical Ginzburg-Landau equation, so was it equally puzzling to find that the pulses were motionless, contrary to expectations based on this equation and on more general symmetry arguments. The present observations of drifting pulses resolve this puzzle and reopen the possibility that such a model can explain the quantitative features of traveling-wave pulses. However, it must be recognized that, be-

cause of the large-scale concentration flows revealed in numerical pulses [11], it is probably erroneous to assume that traveling-wave pulses represent only an infinitesimal perturbation of the conducting state. A symptom of this is that observed pulse velocities are small $-v_{dr} \lesssim 0.1$, while the group velocity s in the Ginzburg-Landau equation for the weakly nonlinear case has a typical value of 1.5 for the fluids used in these experiments. Thus the Ginzburg-Landau model which pertains to experimental pulses may be ill suited for a first-principles quantitative calculation based on a perturbation analysis of the Navier-Stokes equations.

If a phenomenological Ginzburg-Landau model can be constructed which explains pulse drift and shape in detail, then it will face three interesting new tests: to explain first the interactions between pulses and fast TW fluctuations that were described in Ref. [7]; second, the pulse-pulse collisions described there and in Ref. [19], and, third, the intrinsic destabilization described here. I have reserved all discussion of pulse collisions for Ref. [19]. In both of the other two phenomena, TW's with vastly different wave speeds must be described. The strong hysteresis, apparently arbitrary length, and small-to-vanishing phase velocities encountered in the intrinsic destabilization process are major features which may be quite difficult to explain on the basis of this theory or any other. It is worth pointing out that a very similar destabilization scenario, characterized by a slow expansion into the rest of the system, a strong decrease in wave speed, and absence of spatiotemporal defects, has been reported in experiments on confined states in rectangular cells at separation ratios closer to zero [20,29]. In those experiments, the destabilization was shown to be the result of a transition from a convectively unstable situation to an absolutely unstable one. In the present work, however, the estimate of the absolute instability threshold based on the Ginzburg-Landau equation appropriate to the weakly nonlinear case—which may be quantitatively incorrect at the present values of ψ —suggests that the destabilization reported in Figs. 20 and 21 takes place far

below this transition. For this reason, I have referred to this process as “intrinsic.”

It should also be pointed out that the intrinsic destabilization seen in the present annular geometry is qualitatively different in some respects from that seen at comparable ψ in a rectangular cell with suppressed fluctuations [8]. Here, for $\psi = -0.072$, the expansion of the edges of the pulse into the rest of the system is accompanied by a strong decrease in phase velocity, while spatiotemporal defects are not seen [30]. In a rectangular cell with $\psi = -0.089$, the phase velocities in the stable and unstable pulses were essentially the same, and spatiotemporal defects were common. These differences may be related to end-wall reflections or the different cell widths.

Finally, there remains one issue which may be resolved by further experimentation. The numerical computations of Ref. [11] suggest an intimate connection between the pulses described here and the confined states of arbitrary length which were observed some time ago at more negative values of ψ [23]. Both confined states are accompanied by the large-scale concentration flow mentioned in the preceding paragraphs, which slows their drift from the velocity of the underlying TW to the low values observed in these experiments. However, the original observations of the arbitrary-length states found them to be motionless in annular containers [23], while these states were observed to drift *backwards* in subsequent experiments in rectangular containers, independent of the direction of stray gradients in $\epsilon(x)$ [31]. The drift of those confined states does not seem to be as clearly related to cell nonuniformities as it is in the case of TW pulses. New experiments in a very uniform cell are needed to resolve this situation.

ACKNOWLEDGMENTS

I thank P. C. Hohenberg, M. Lücke, C. M. Surko, and J. D. Crawford for useful discussions and B. L. Winkler for many instances of helpful advice and assistance.

-
- [1] E. Moses, J. Fineberg, and V. Steinberg, *Phys. Rev. A* **35**, 2757 (1987); R. Heinrichs, G. Ahlers, and D. S. Cannell, *ibid.* **35**, 2761 (1987).
 - [2] J. J. Niemela, G. Ahlers, and D. S. Cannell, *Phys. Rev. Lett.* **64**, 1365 (1990).
 - [3] K. E. Anderson and R. P. Behringer, *Phys. Lett. A* **145**, 323 (1990).
 - [4] M. C. Cross, *Phys. Rev. Lett.* **57**, 2935 (1986).
 - [5] O. Thual and S. Fauve, *J. Phys. (Paris)* **49**, 1829 (1988); O. Thual and S. Fauve, *Phys. Rev. Lett.* **64**, 282 (1990).
 - [6] W. van Saarloos and P. C. Hohenberg, *Phys. Rev. Lett.* **64**, 749 (1990), and (unpublished).
 - [7] P. Kolodner and J. A. Glazier, *Phys. Rev. A* **42**, 7504 (1990); J. A. Glazier and P. Kolodner, *ibid.* **43**, 4269 (1991).
 - [8] P. Kolodner, *Phys. Rev. A* **43**, 2827 (1991).
 - [9] G. Ahlers, *Physica D* **51**, 421 (1991).
 - [10] H. R. Brand and R. J. Deissler, *Phys. Rev. Lett.* **63**, 2801 (1989); R. J. Deissler and H. L. Brand, *Phys. Lett. A* **146**, 252 (1990).
 - [11] W. Barten, M. Lücke, and M. Kamps, *Phys. Rev. Lett.* **66**, 2621 (1991).
 - [12] I have made a preliminary report of these results: P. Kolodner, *Phys. Rev. Lett.* **66**, 1165 (1991).
 - [13] The height uniformity achieved in cell *C* was a bit worse than this, and, because of a poorly seated gasket, cell *B* was substantially worse. However, in all three cells, nonuniformities in the applied temperature difference, rather than in the cell geometry, appeared to be the dominant cause of nonuniformity in the Rayleigh number (see Secs. III and IV for details).
 - [14] P. Kolodner, H. Williams, and C. Moe, *J. Chem. Phys.* **88**, 6512 (1988).
 - [15] P. Kolodner and H. Williams, in *Proceedings of the NATO Advanced Research Workshop on Nonlinear Evolution of Spatio-temporal Structures in Dissipative Continuous Systems*, Vol. 225 of *NATO Advanced Study Institute Series B2*, edited by F. H. Busse and L. Kramer (Plenum, New

- York, 1990), p. 73.
- [16] C. M. Surko and P. Kolodner, *Phys. Rev. Lett.* **58**, 2055 (1987); P. Kolodner, C. M. Surko, H. L. Williams, and A. Passner, in *Propagation in Systems Far from Equilibrium*, edited by J. E. Wesfreid *et al.* (Springer-Verlag, Berlin, 1988), p. 282; P. Kolodner, C. M. Surko, and M. C. Cross (unpublished).
- [17] M. C. Cross and K. Kim, *Phys. Rev. A* **37**, 3909 (1988); S. J. Linz and M. Lücke, *ibid.* **35**, 3997 (1987); B. J. A. Zie-linska and H. R. Brand, *ibid.* **35**, 4349 (1987); E. Knobloch and D. R. Moore, *ibid.* **37**, 860 (1988).
- [18] The dependences on cell width of the critical wave number, of Hopf frequency, and onset Rayleigh number are presently being measured in a long rectangular cell: P. Kolodner (unpublished).
- [19] P. Kolodner, following paper, *Phys. Rev. A* **44**, 6466 (1991).
- [20] V. Steinberg and E. Kaplan, in *Proceedings of the NATO Advanced Research Workshop on Spontaneous Formation of Space-Time Structures and Criticality, NATO Advanced Study Institute Series B2*, edited by T. Riste and D. Sherington (Plenum, New York, in press).
- [21] P. Kolodner, *Phys. Rev. A* **42**, 7204 (1990).
- [22] W. Schöpf and I. Rehberg, *Europhys. Lett.* (to be published); I. Rehberg, S. Rasenat, M. de la Torre Juarez, W. Schöpf, F. Hörner, G. Ahlers, and H. R. Brand, *Phys. Rev. Lett.* **67**, 596 (1991).
- [23] P. Kolodner, D. Bensimon, and C. M. Surko, *Phys. Rev. Lett.* **60**, 1723 (1988).
- [24] C. M. Surko, D. R. Ohlsen, S. Yamamoto, and P. Kolodner, *Phys. Rev. A* **43**, 7101 (1991).
- [25] M. Lücke (private communication).
- [26] W. Schöpf and W. Zimmerman, *Europhys. Lett.* **8**, 41 (1989).
- [27] P. Kolodner, J. A. Glazier, and H. Williams, *Phys. Rev. Lett.* **65**, 1579 (1990); J. A. Glazier, P. Kolodner, and H. Williams, *J. Stat. Phys.* **64**, 945 (1991).
- [28] W. Schöpf and L. Kramer, *Phys. Rev. Lett.* **66**, 2316 (1991).
- [29] C. M. Surko and P. Kolodner, in *Nonlinear Structures in Physical Systems*, edited by L. Lam and H. C. Morris (Springer-Verlag, New York, 1990), p. 147. Figure 4 in this paper illustrates the convective-absolute transition in a rectangular cell of length 16.625 at $\psi = -0.021$.
- [30] This same scenario has also been seen in recent experiments at $\psi = -0.12$: P. Kolodner (unpublished).
- [31] P. Kolodner, *Phys. Rev. A* **42**, 2475 (1990); P. Kolodner (unpublished).